

“Interaction-free” imaging

Andrew G. White,* Jay R. Mitchell, Olaf Nairz,[†] and Paul G. Kwiat
 Los Alamos National Laboratory, P-23, MS-H803, Los Alamos, New Mexico 87545

(Received 19 December 1997)

Using the complementary wavelike and particlelike natures of photons, it is possible to make “interaction-free” measurements where the presence of an object can be determined with no photons being absorbed. We investigated several “interaction-free” *imaging* systems, i.e., systems that allow optical imaging of photosensitive objects with less than the classically expected amount of light being absorbed or scattered by the object. With the most promising system, we obtained high-resolution (10- μm), one-dimensional profiles of a variety of objects (human hair, glass and metal wires, and cloth fibers) by raster scanning each object through the system. We discuss possible applications and the present and future limits for interaction-free imaging. [S1050-2947(98)07906-2]

PACS number(s): 42.50.Ct, 03.65.Bz, 42.25.Hz, 03.67.-a

I. INTRODUCTION

For most of us, our intuition of how the world works is grounded in everyday experience and so is necessarily classical. Since its earliest days, the field of quantum mechanics has been characterized by predictions and apparent paradoxes that run counter to our natural intuition. However, in remarkably short order, the practitioners of quantum mechanics developed new intuitions [1]. One of the widely accepted tenets of this new intuition is that in quantum mechanics every measurement of a system disturbs the state of that system (unless the system is already in an eigenstate of the measurement observable).

Yet over the years a number of works have tested this intuition. In 1960 Renninger showed that the state of a quantum system could be determined via the *nonobservance* of a particular result, i.e., the absence of a measurement or observation can lead to definite knowledge of the state of the system [2]. In 1981 Dicke considered “*interaction-free quantum measurements*” where energy and/or momentum is transferred from a photon to a quantum particle by the *non-scattering* of the photon by the particle [3]. In 1993 Elitzur and Vaidman [4] showed that an arbitrary object (classical or quantum) can affect the interference of a single quantum particle with itself—the *noninterference* of the particle allows the presence of the object to be inferred without the particle and object ever directly “interacting” [5]. In the Elitzur-Vaidman (EV) interaction-free measurement (IFM) scheme, the measurement is interaction-free at most half of the time. Such experiments were reported in 1995 by Kwiat *et al.* [6] and later repeated as part of a public demonstration in the Netherlands [7]. References [6,8] also proposed several schemes for high-efficiency IFM’s: The fraction of IFM’s exceeds one-half and in principle can be made arbitrarily close to unity, i.e., the probability of absorption can be made arbitrarily close to zero. In an experiment using a high-

efficiency system, Kwiat *et al.* demonstrated the feasibility of performing IFM’s up to 85% of the time [9]. The possibility of detecting the presence of an object without *ever* interacting with it led to the suggestion of *interaction-free imaging* (IFI) [10], e.g., optical imaging of photosensitive objects with much less than the classically expected amount of light being absorbed or scattered by the object. As one of the current limitations to imaging biological systems is power-induced optical damage, the possibility of evading this limitation via interaction-free imaging bears further investigation.

While we realize that the best advantage of IFM techniques is realized in high-efficiency schemes, for the sake of conceptual and experimental simplicity, we consider in this paper only devices based on the EV scheme, that is, intrinsically low-efficiency devices. Specifically, we describe investigations of several possible interaction-free imaging devices, present experimental results from the most promising of these, and explore present and future limits to practicable IFI devices. With these preliminary devices we obtained one-dimensional profile images: The objects were raster scanned through the beam of an interaction-free measurement system. To obtain high spatial resolution, the beam at the imaging point is focused to a small size.

Figure 1 shows the canonical EV scheme: a single photon sent through a Mach-Zehnder interferometer. The interferometer is set so that if no object is present, all of the light is output to port 1 and none to port 2. [Complete destructive interference is always possible if the transmittance (reflec-

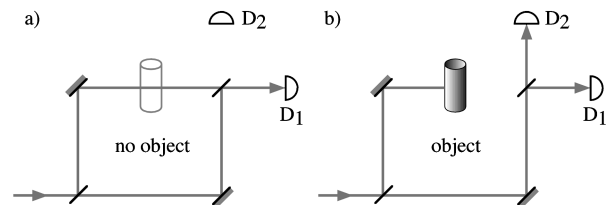


FIG. 1. Elitzur-Vaidman scheme for interaction-free measurements: (a) no object, the photon interferes with itself and no counts are detected at D_2 , and (b) an object in one arm of the interferometer, the interference is destroyed and counts are detected at D_2 (one-quarter of the time for 50-50 beam splitters).

*FAX: +1 (505) 665 4121. Electronic address: andrew.white@lanl.gov

[†]Present address: Institut für Experimentalphysik, Universität Innsbruck, Technikerstrasse 25, 6020 Innsbruck, Austria.

tance) of the recombining beam splitter equals the reflectance (transmittance) of the first beam splitter.] The probability of photon counts at detector 1 is thus unity, while that at detector 2 is zero, i.e., $P(D_1)=1$ and $P(D_2)=0$. If an opaque object is placed in one arm of the interferometer the interference is destroyed. The probability of the photon being reflected by the first beam splitter and thus directed onto and being absorbed by the object is $P_{\text{abs}}=R_1$. The probability of detection at detector 1, i.e., the photon being transmitted by the first beam splitter and reflected by the second beam splitter, is $P(D_1)=T_1R_2$. Note that in this *no-result* case we gain no information on the presence of the object: This detector can fire whether or not the object is there. (The high-efficiency schemes do not suffer this ambiguity [6,9].) The probability of detection at detector 2, i.e., the photon being transmitted through both beam splitters, is $P(D_2)\equiv P_{\text{IFM}}=T_1T_2$ (we label detector 2 the IFM detector: $D_2\equiv D_{\text{IFM}}$). On the occasions that detector 2 fires we know that there is an object in the interferometer arm and we know that no photon was absorbed since we only sent a single photon into the interferometer. The presence of the object has been determined without direct interaction between the detected photon and the object.

The ‘‘efficiency’’ of an IFM device, that is, how often the device is likely to make an interaction-free as opposed to an interaction-full measurement, is defined as [6]

$$\eta = \frac{P_{\text{IFM}}}{P_{\text{IFM}} + P_{\text{abs}}}. \quad (1)$$

Assuming lossless beam splitters, in the EV system considered here this becomes

$$\eta = \frac{T_1T_2}{T_1T_2 + R_1}. \quad (2)$$

If we add the condition that the transmittance of the second beam splitter is $T_2=R_1$, then

$$\eta = \frac{T_1}{1+T_1} = \frac{1-R_1}{2-R_1} \quad (3)$$

and we see that $\eta \rightarrow 0.5$ as $R_1 \rightarrow 0$. Note that no-result measurements (from detector 1) are not considered, as we do not mind if a photon propagates through the system and is neither absorbed by the object nor detected at detector 2. For a balanced interferometer, where $R_1=T_2=0.5$ and the intensities in both arms are equal, the probability of an interaction-free measurement is at a maximum, $P_{\text{IFM}}=0.25$; however, the efficiency is only $\eta=0.33$: As the efficiency increases there are more no-result measurements and the probability of an IFM measurement actually decreases. We stress that regardless of the efficiency, when a single photon is detected at detector 2, that particular measurement is *completely interaction-free*, as the object has been detected yet the photon was not absorbed by the object. The efficiency only relays the *ratio* of interaction-free to interaction-full and interaction-free measurements: Each *individual* single photon measurement is either no-result, interaction-free, or interaction-full.

Single-photon experiments are more demanding than typical continuous wave (cw) experiments in that they require special detectors, very low background light levels, and so on. Fortunately, it is not necessary to use single photons to analyze and compare various interaction-free imaging schemes. The probability P_{event} of a detection event in the single-photon regime is related to the relative intensity of that event in the cw regime:

$$P_{\text{event}} = \frac{\mathcal{P}_{\text{event}}}{\mathcal{P}_0}, \quad (4)$$

where \mathcal{P}_0 is the cw power incident to the interferometer and $\mathcal{P}_{\text{event}}$ is the cw power detected at the event port (i.e., port 1 or 2, or absorbed by the object). All the experiments presented in this work were done in the cw regime. Obviously, in this regime no measurement is interaction-free: With many photons simultaneously incident on the interferometer some can be absorbed by the object while others can exit via port 2. However, according to the standard rules of quantum mechanics, by measuring the relative intensity of light at a given port [as described in Eq. (4)] we can calculate the probability of an event at that port in the single-photon regime. In other words, our evaluations in the cw regime should be identical if performed with a single-photon source and detectors.

II. EXPERIMENTS

A. Imaging systems

Interaction-free imaging requires an instrument with high-contrast interference, in order to give low-noise interaction-free measurements, and an accessible and small beam waist, to allow fine resolution raster scanning of an object. In all, four imaging systems were investigated experimentally. The first three systems were variations on a Michelson interferometer (Fig. 2), the last a Mach-Zehnder interferometer (Fig. 3). For all systems the imaging beam was the output of a diode laser (1 mW at 670 nm, Thor Labs, Model 0220-999-0, circular output beam) that was expanded and collimated by a telescope and then apertured with an iris. The detector was a calibrated photodetector (Newport 818-UV, used with a 1835-C power meter).

The first imaging system was a Michelson interferometer with two lenses ($5\times$ microscope objectives) [Fig. 2(a)]. This design had an accessible beam waist between the two lenses. Unfortunately, in practice, it had very poor fringe visibility, as the system was very sensitive to alignment mismatch between the lenses (due to coma, astigmatism, etc.). Given the poor performance, no data were taken with this system.

The second system was a Michelson interferometer with a single lens in the imaging arm, focused so that the waist was at the end mirror [Fig. 2(b)]. As the beam was spatially inverted in the imaging arm, but not the other, it was still difficult to get high fringe visibility since we did not have the necessary, highly spatially symmetric, wave front. Further, the waist was no longer easily accessible: Due to mechanical constraints, in practice, it was only possible to get an object to within $\sim 200 \mu\text{m}$ of the waist. Again, no data were taken with this system.

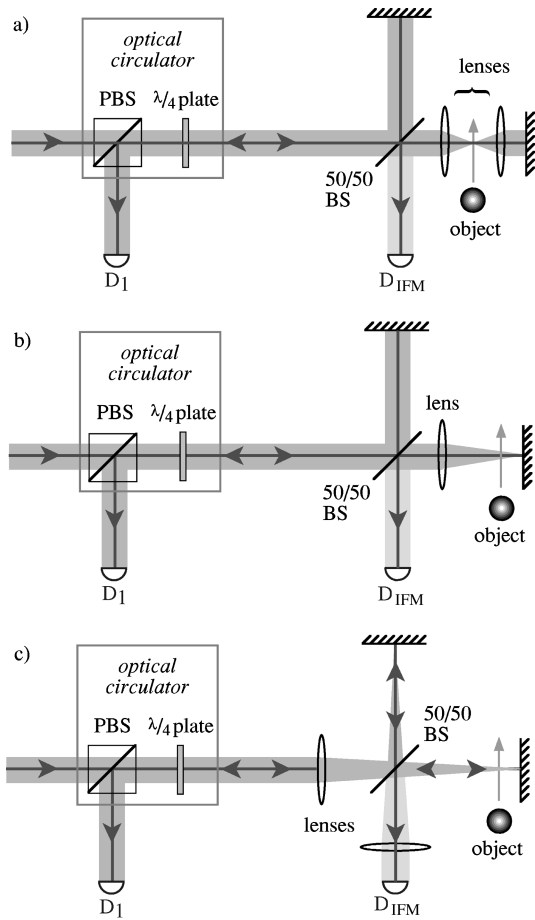


FIG. 2. Conceptual layout of three interferometer configurations: (a) Michelson interferometer with two lenses in the imaging arm and the focus in free space, (b) Michelson interferometer with one lens in the imaging arm and the focus at the end mirror, and (c) Michelson interferometer with no lenses in the interferometer. The beam splitters are all $R=0.5$, so the maximum possible interaction-free efficiency in these configurations is $\eta=0.33$.

In the third system the lens was removed from within the interferometer and placed before the first beam splitter [Fig. 2(c)]. This was the best of the three Michelson systems that we considered, in that it had good fringe visibility (in excess of 90%) because both beams undergo the same spatial inversion at their respective mirrors. However, as for system 2, it is not possible to image exactly at the waist.

The Michelson systems were investigated chiefly because of the perceived advantages of their relative ease of alignment. However, regardless of the exact configuration, they all have one feature that complicates interpretation of imaging data: The beam passes through the object *twice*. If the object is semitransparent, then twice the actual loss is experienced and still further analysis of an image is required. Furthermore, a subtle effect means that any data from system 2 or 3 must be very carefully interpreted. Consider the following argument. In system 3 [Fig. 2(c)] let half the beam be blocked in the imaging arm at a point just after the beam splitter. The remaining half of the beam is focused onto the end mirror and returns on the *other* side of the beam, where it too is absorbed by the initial block. Thus, by blocking only half the beam in the imaging arm, all the light in that arm is absorbed (neglecting diffraction) and the interference is to-

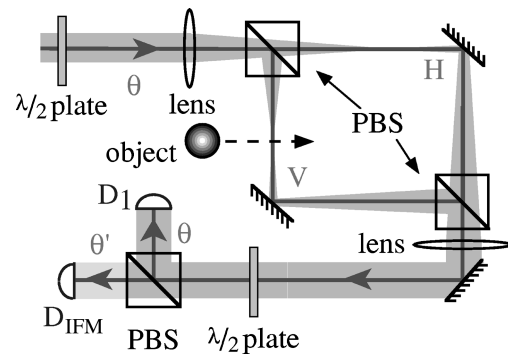


FIG. 3. Polarizing Mach-Zehnder interferometer. PBS denotes the polarizing beam splitter and $\lambda/2$ the half-wave plate at 670 nm. The locking laser (not shown) entered from the top port of the first PBS and exited from the side port of the second.

tally destroyed. This effect does not occur if the beam is blocked at the waist. However, as mentioned above, we could not image precisely at the waist. In system 3 we typically imaged at around one Rayleigh range, i.e., in a region somewhere between the far field and the waist, meaning that this half-beam effect is occurring to some degree. The interpretation of the data is then nontrivial: A full calculation accounting for the double Fresnel edge-diffraction would be necessary.

The fourth imaging system was a Mach-Zehnder configuration, used to obtain all the data presented here. With this system it is easy to arrange for an accessible beam waist in free space and the beam only passes through the object once. Further, it was experimentally necessary to lock the interferometers so that one port, the IFM port, was at a null. This was done with an additional laser (a He-Ne laser at 632 nm) and a simple fringe slope locking system. Incorporation of the locking laser into a Michelson configuration was difficult due to the intrinsic space constraints of that design; incorporation into a Mach-Zehnder configuration was trivial—the empty ports of the interferometer were utilized.

Figure 3 shows the Mach-Zehnder configuration: a *polarizing* interferometer, which allows effective tuning of the beam-splitter reflectances. This configuration operates as follows. The first half-wave plate ($\lambda/2$) is set so that the light input to the interferometer is linearly polarized at θ from the vertical axis. The first polarizing beam splitter (PBS) splits the light into its horizontal ($T_1 = \sin^2 \theta$) and vertical ($R_1 = \cos^2 \theta$) components (for example, $\theta=45^\circ$ gives $R_1 = 0.5$). If no object is present, the second PBS recombines the beams to the original θ polarization, which then is rotated back to the vertical by the second $\lambda/2$ plate, so that the light is always detected at D_1 . If an object is present, however, the interference is modified or destroyed. In the latter case, only the horizontal component is transmitted by the interferometer, the vertical component being absorbed by the object. (In quantum terms, only the probability amplitude of the horizontal polarization path contributes to the final probabilities.) The horizontally polarized output is rotated towards the vertical axis by the second $\lambda/2$ plate, so that some counts occur at D_{IFM} ($T_2 = \cos^2 \theta$): These counts are the interaction-free measurements. As with the most successful Michelson system, the focusing lens ($f=60$ mm) was outside the interference region.

TABLE I. Object widths: inferred from “interaction-free” and normalized transmission scans, measured with microscope and diffraction. The uncertainty of the widths from the IFM and transmission scans are approximately $\pm 1\%$, except for the cloth filament where they are approximately $\pm 2\%$.

Object	Width inferred from IFM scan (μm)	Width inferred from transmission scan (μm)	Width measured by microscope (μm)	Width measured via diffraction (μm)
Thin metal wire	95.3	96.6	95.5 ± 1.6	97.0 ± 0.5
Thick metal wire	160.2	162.7	159.1 ± 2.3	159.5 ± 2.0
Cloth filament	16.6	16.3	12.6 ± 0.6	15.4 ± 1.2
Human hair filament	22.8	24.7	25.1 ± 0.9	26.2 ± 0.6
Thin optical fiber	125.7	123.9	123.5 ± 1.9	123.2 ± 3.6
Thick optical fiber	208.0	207.5	207.9 ± 3.0	208.3 ± 2.5
Slit	12.5	13.1	N.A.	19.2 ± 1.2

B. Imaging results

We performed one-dimensional scans of a variety of different objects, including a simple knife-edge, human hair, metal wire, cloth and optical fibers, and a narrow slit (the absence of an object) (see Table I). Typical results are shown in Fig. 4, these being obtained for $R \approx 0.5$, i.e., input light polarized at $\approx 45^\circ$ and analyzing at $\approx -45^\circ$.

The objects were scanned stepwise through the beam using a motorized translation stage incorporating a high-resolution ($0.0555\text{-}\mu\text{m}$) encoder. At each step two measurements were recorded: The first was an interaction-free measurement, monitoring the dark port of the interferometer (analyzing at -45°) for an inhibition of the interference, and the second measurement was a normalized transmission scan obtained by blocking the interferometer arm that did not contain the object and measuring at the no-result port (detector D_1). These are, respectively, the left-hand (P_{IFM}) and right-hand (P_{norm}) ordinates of Fig. 4. Note that P_{norm} is the probability of a photon being transmitted through the object *outside* the imaging system, i.e., just the normal transmittance curve for the object. The probability that a photon is absorbed by the object when it is in the imaging system is given by P_{abs} , where

$$P_{\text{abs}} = R_1[1 - P_{\text{norm}}]. \quad (5)$$

The knife-edge profile [Fig. 4(a)] is used to measure the resolution of the system. Since the knife-edge certainly has a step-function profile on the micrometer scale, the rounding of the edges on the scans is necessarily due to the spot size of the beam. Taking the derivative to obtain a Gaussian-like function, we infer a full width at half maximum (FWHM) spot size of $9.1 \pm 0.3 \mu\text{m}$. The Rayleigh resolution of the system is thus given by $10.7 \pm 0.3 \mu\text{m}$ [11]. The difference between this and the theoretical value of $d = 9.8 \mu\text{m}$ (see Appendix A) is probably due to the nonideal beam quality: Despite aperturing down, the beam was still not entirely spatially uniform.

The path of the knife-edge through the beam is shown by the transmission scan: The beam was initially unblocked ($x < 60 \mu\text{m}$) and the knife-edge was scanned through until the beam was totally blocked ($x > 130 \mu\text{m}$). In principle, $P_{\text{IFM}} = 0$ in the absence of the knife-edge; however, in practice, it

is not, as shown by the value $P_{\text{IFM}} = 0.035$ in Fig. 4(a). This background noise is from light leaking through the “dark” port due to the imperfect fringe visibility ($V = 0.933$ for this scan) and can be thought of as the “dark noise” σ of the interaction-free detector [for this scan $\sigma = (1 - V)/(1 + V) = 3.5\%$]. For the remainder of the scans, the visibility was improved to reduce the noise, which varied between 2.0% and 3.2%.

In the simple Mach-Zehnder EV scheme described in the Introduction, the IFM probability is set by the transmittance of the two beam splitters in the interferometer; in the polarizing Mach-Zehnder this is instead the transmittance of the first polarizing beam splitter and the transmittance of the analyzing beam splitter after the second half-wave plate. The exact values of these transmittances for a given experiment can be inferred from the ratios of measurements at D_1 and D_{IFM} for both the transmission and the IFM scans when the object is fully blocking the beam. Recall that when an object is fully blocking the beam the expected IFM probability is the product of these transmittances. For the knife-edge scans $T_1 = 0.467$, $T_2 = 0.422$, and so $P_{\text{IFM}}^{\text{th}} = 0.23$, in good agreement with the observed value of $P_{\text{IFM}} = 0.22 \pm 0.01$ on the right-hand side of the IFM scan in Fig. 4(a) (the error on each data point in the IFM scans is typically $\pm 4\%$ of the value of that point).

Figure 4(b) is a profile of a metal wire. The diameter (FWHM) of the wire was estimated from both the transmission ($96.6 \pm 1.0 \mu\text{m}$) and IFM ($96.6 \pm 1.0 \mu\text{m}$) scans and was in good agreement with the width measured via a microscope ($95.5 \pm 1.6 \mu\text{m}$) and diffraction of a laser beam ($97.0 \pm 0.5 \mu\text{m}$). A larger wire was also scanned (not shown) and again agreement between the transmission ($162.7 \pm 1.6 \mu\text{m}$), IFM ($160.2 \pm 1.6 \mu\text{m}$) scans, microscope ($159.1 \pm 2.3 \mu\text{m}$), and diffraction measurements ($159.5 \pm 2.0 \mu\text{m}$) was very good. This gives us confidence that the system can be used to accurately profile opaque objects at this scale.

For these scans the transmittances were adjusted ($T_1 = 0.525$ and $T_2 = 0.462$) to give a higher expected IFM probability, $P_{\text{IFM}}^{\text{th}} = 0.24$. Again this agrees with the actual IFM values observed in the center of the IFM scan where the wire totally obscures the beam. The efficiency of the measurement

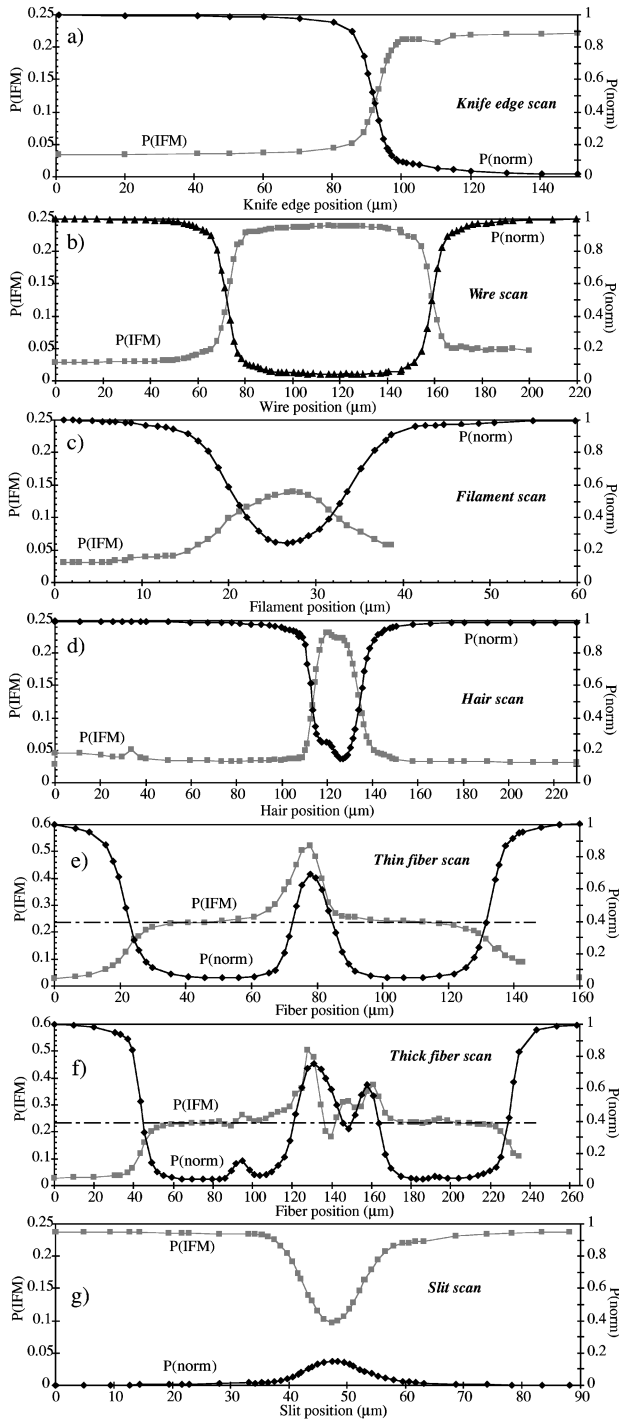


FIG. 4. Transmission and interaction-free images of various objects: (a) knife-edge, (b) metal wire, (c) cloth filament, (d) human hair, (e) thin optical fiber, (f) thick optical fiber, and (g) slit (the absence of an object). Note the variation in scale on position axes.

in the central region can be calculated directly from Eq. (2); we obtain $\eta=0.34$. Alternatively, η can be calculated via Eq. (1); however, this requires the probability of absorption P_{abs} , which was not measured directly. Fortunately, P_{abs} can be calculated from the measured value of the normalized probability of transmission [see Eq. (5)]. In the central region $P_{\text{abs}}=0.46$, again giving an experimental efficiency of $\eta=0.34$. The agreement between the efficiency calculated only from the reflectances and the efficiency calculated using

the inferred absorption probability gives us confidence in the experimental analysis.

Note that the noise on the IFM scan rises slightly towards the right-hand side of the scan and that the IFM scan terminates before the transmission scan. This behavior is due to the nonideal lock of the interferometer: The system gradually drifted away from the dark fringe, increasing the light and thus the noise through the dark port, before finally losing lock, ending the IFM scan. This behavior is seen on several of the scans [Figs. 4(b), 4(c), 4(e), and 4(f)] and highlights the importance of a robust locking scheme in future IFI systems.

Figure 4(c) is a profile of a cloth fiber. The FWHM diameter was measured to be $12.6 \pm 0.6 \mu\text{m}$ (microscope) and $15.4 \pm 1.2 \mu\text{m}$ (diffraction), respectively. The difference between these two measurements suggests that the fiber had a nonuniform or nonisotropic (e.g., elliptical) cross section and that different sections or orientations of the fiber were measured by the two different techniques, giving slightly different widths. This is further borne out by the FWHM diameters measured from the transmission and IFM scans ($16.3 \mu\text{m}$ and $16.6 \mu\text{m}$, respectively): They are consistent with one another, are within one standard deviation of the diffraction measurement, and differ significantly from the microscope measurement.

A more important feature of this scan is that as the transmission never drops to zero (i.e., the cloth fiber is not fully opaque), the probability of an interaction-free measurement never attains its maximum value of one-quarter. At the minimum of transmission, $P_{\text{norm}}=0.24$, from which we expect $P_{\text{IFM}}^{\text{th}}=0.07$ (see Appendix B for calculating P_{IFM} from P_{norm}). Actually, the observed value was higher than this, $P_{\text{IFM}}=0.14$. A similar discrepancy is seen in the profile of a human hair [Fig. 4(d)]. Note the internal structure of the traces. As can be seen from the transmission scan, the hair is also not totally opaque [the transmission never falls to zero; cf. scans in Figs. 4(a) and 4(b)] and, furthermore, near the center of the hair ($x \approx 119 \mu\text{m}$) more light is transmitted than at the edges, particularly the right edge ($x = 123 \mu\text{m}$). Left of center, where the object is less opaque and there is seemingly less chance of an IFM, one might expect the IFM scan to drop accordingly; however, it clearly *increases*. This is even more striking in the profile of a thin optical fiber, as shown in Fig. 4(e). Here, for two-thirds of the width of the fiber, the fiber is essentially opaque (due to scattering and reflection from the curved surface of the fiber) and P_{IFM} is near the expected value of $P_{\text{IFM}}^{\text{th}}=0.23$. However, in the middle of the fiber the transparency increases notably and P_{IFM} attains values of up to 0.52, exceeding even the naive in-principle limit of 0.25.

In all three cases [the scans in Figs. 4(c)–4(e)] we believe the increase in P_{IFM} is caused by the light transmitted through the object acquiring a relative phase shift, which changes the interference conditions and so causes the IFM port to no longer be at a dark fringe. This is clearly an important phenomenon in IFM measurements (and, in fact, is present to an even greater degree in high-efficiency schemes [9]). Consider, for example, imaging a completely transparent object ($P_{\text{norm}}=1$ and $P_{\text{abs}}=0$) that introduces a π -phase shift: All the light is detected at the “dark” port detector yielding a 100% efficiency, i.e., $P_{\text{IFM}}=1$ and $\eta=1$. As the

transparency of such an object is reduced, then P_{IFM} and η decrease accordingly. In the limit where the object is totally opaque we recover our familiar results of $P_{\text{abs}}=R_1$, $P_{\text{IFM}}=T_1T_2$, and η as given by Eq. (3). As soon as there is some probability that a photon can be transmitted through the object, it is no longer sensible to describe the measurements as interaction-free and concepts and equations based on the assumption of detecting a wholly opaque object need to be used with care (see Sec. III).

However, what exactly causes the phase shift? As shown by the asymmetry of the IFM scan in Fig. 4(e) it is clearly associated with, but not directly proportional to, the increase in transparency. There are several possible causes for both the phase and transparency shifts: scattering and reflection from the object, the phase shift due to passage through the object ($\phi=[2\pi(n-1)D]/\lambda$, where D is the width of the object that the light passes through), and the geometrical phase shift due to the additional focusing from a semitransparent cylinder (i.e., the Guoy phase shift associated with focused beams; approximately π radians [12]). In Fig. 4(e) $P_{\text{norm}}=0.69$, from which we expect $P_{\text{IFM}}^{\text{th}}=0.007$ if there were no phase shift (see Appendix B). As the experimental value is $P_{\text{IFM}}=0.52$, we calculate, using Eq. (B6), that the relative phase shift for light passing through the center of the fiber is 104° .

It is tempting to interpret the transmission scan of Fig. 4(e) as a straightforward image of the well-known internal structure of an optical fiber, i.e., a core cylinder of glass surrounded by a cladding cylinder of higher refractive glass. However, given the opportunity for refraction and beam steering, things are not likely to be so straightforward, as borne out by the profile of a thicker optical fiber in Fig. 4(f). Here there are four peaks in the transmission scan (two central and two small side peaks) and four corresponding features in the IFM scan. These are most likely due to guided and scattered light paths and certainly do not represent a simple profile of the core structure. The shape of the features in the IFM scan reflect that the phase shift across the transmission peaks is large and nonuniform.

Finally, Fig. 4(f) is the profile of the *absence* of an object, i.e., a slit. The slit was constructed by aligning two razor-blade edges in close proximity. Due to mechanical constraints, the blade edges were not exactly parallel and the slit was marginally V shaped. From the transmission and IFM scans, we respectively infer slit widths of 13.1 and 12.5 μm and from the diffraction measurement, a width of $19.2 \pm 1.2 \mu\text{m}$. It is probable that the difference was due to a slightly different vertical alignment of the slit with respect to the beam. Note that this, combined with a small longitudinal shift from the waist position, may also explain the surprisingly low transmission (the slit was effectively nearly opaque). The IFM scan is sensitive to small changes in the effective transparency of the object: When the object fully blocks the beam, $P_{\text{norm}}=0$ ($P_{\text{abs}}=0.49$) and P_{IFM} is at its maximum value $P_{\text{IFM}}=0.24$; a small change in the transparency, to $P_{\text{norm}}=0.15$ and $P_{\text{abs}}=0.43$, leads to a much larger change in the IFM scan, $P_{\text{IFM}}<0.097$ (which agrees within error with the expected value $P_{\text{IFM}}^{\text{th}}=0.094 \pm 0.007$). This sensitivity to small changes in transparency holds promise for high-relief interaction-free imaging of low-relief absorption objects, with much less than the classically necessary

light flux. The effect is in fact more pronounced in high-efficiency schemes, wherein it is possible for a given absorptive object to have a *lower* probability of absorption than another object with *lesser* intrinsic absorptance [9].

As a final note, we point out that it may be possible to use the current device to obtain information on the polarization properties of objects. As currently used, the object is interaction-free imaged by purely vertically polarized light (i.e., s polarized with respect to vertically aligned objects); equally validly, interaction-free imaging could be done in the complementary arm with horizontally polarized light (i.e., p polarized with respect to vertically aligned objects). Fine polarization-dependent details could then be brought out by looking at the difference between the two interaction-free images.

C. Approaching high efficiency

In principle, the measurements in the preceding subsection could have been made at efficiencies higher than $\eta=0.33$ (up to $\eta=0.5$ in the EV scheme). However, there was a strong experimental reason why this was not done. As discussed previously, the probability of an IFM in the EV scheme is actually highest when $R_1=T_2=0.5$, i.e., $P_{\text{IFM}}=0.25$ and $\eta=0.33$. Because the IFM noise floor is a fixed value set by the visibility of the interferometer ($\sigma \sim 2-3\%$ for our system) the greatest signal-to-noise ratio (and so the greatest detail) for IFM scans is attained when $P_{\text{IFM}}=0.25$.

To investigate this issue, P_{IFM} and efficiency were measured for a range of reflectances. An opaque object completely blocked the imaging arm of the polarizing Mach-Zehnder interferometer. By appropriately varying the angles of the two half-wave plates (see Fig. 3) the reflectances were varied so that $R_1=T_2 \equiv R$, where $0 < R < 1$. The results are shown in Fig. 5. For high reflectances, $P_{\text{IFM}} \simeq \eta$, as the probability of absorption is very high. P_{IFM} attains its maximum value at $R=0.5$; in the region $0.5 < R < 1$, P_{IFM} decreases because the probability of a no-result measurement increases. (The P_{IFM} decrease is not reflected in the efficiency because by definition η depends only on the ratio of P_{IFM} to P_{IFM} and P_{abs} , and P_{abs} also decreases as $R \rightarrow 0$.)

The experimental values of P_{IFM} were calculated directly from the output powers [as described by Eq. (4)]. To obtain the experimental values for efficiency it was necessary to know the values for P_{abs} : These were calculated by assuming that the sum of the absorption, interaction-free, and no-result powers equaled the observed output power in the *absence* of an object. The agreement between experiment and theory for P_{IFM} is excellent.

The agreement for the efficiency is also very good, but breaks down badly at low reflectances, when polarization cross talk degrades the efficiency. Polarizing beam splitters are designed to separate an arbitrarily polarized beam into its horizontal and vertical components. The *cross talk* of a PBS is the residual amount of the orthogonal polarization on each ‘‘pure’’ output beam. Thus at low reflectances, where P_{abs} is in principle vanishingly small, in practice it has a fixed value, set by the cross talk. The undesirable consequence of this is that, while P_{IFM} decreases as $R \rightarrow 0$, P_{abs} is fixed due to the cross talk and thus the efficiency η decreases sharply.

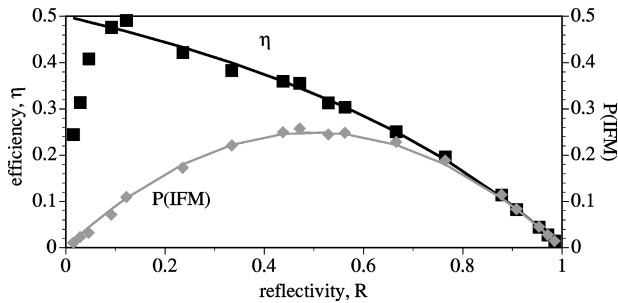


FIG. 5. Efficiency and probability of an interaction-free measurement as a function of reflectance. Diamonds and squares respectively represent experimentally measured values of P_{IFM} and efficiency η . The unbroken lines are the theoretical curves (ignoring the effects of PBS cross talk).

The system only behaves as described by Eqs. (1)–(3) for reflectances above $\sim 10\%$.

III. DISCUSSION

As has been touched upon in Sec. II B, semitransparent objects necessarily force a reevaluation of what is meant by an interaction-free measurement. The original central idea of interaction-free measurement was a totally opaque object causing the noninterference of a single photon [4]. Classical objects can modify this effect if they are semitransparent or diffract the light. A transparent or semitransparent object can phase shift the light and modify the interference (we note in passing that such shifts can in principle yield information about the dispersive properties of the object). However, even in the absence of such a phase shift, some interference will still occur, as any transmitted light may interfere with the light from the other arm of the interferometer. Similarly, even a totally opaque object may allow interference if it diffracts light in such a way that it can overlap with light from the other arm.

Quantum objects may also be imaged by interaction-free detectors [13,14]. For these objects, any forward scattering (be it due to transparency, diffraction, reemission, or some other process) will allow some degree of interference. Further, during interaction-free measurements of quantum objects, momentum and energy can be transferred from the light to the object [3,15] if there is a forward-scattering amplitude from the object. Energy and momentum transfer are unusual phenomena indeed for an “interaction-free” measurement! Accordingly, we reiterate that as soon as there is some probability that a photon can be transmitted or diffracted by the object, it is no longer sensible to describe the measurements as truly interaction-free, at least in the original sense of the phrase.

An interaction-free measuring system can be thought of as a detector, albeit an unusual one. As with all detectors, IFM systems are characterized in terms of their efficiency (η) and noise (σ). The interaction-free imaging systems considered here are extensions of this concept: They are IFM detectors with fine spatial resolution. The ultimate limit to spatial resolution for any standard optical detector is the diffraction limit: In the current system we are still some way from achieving this limit ($\sim 10 \mu\text{m}$ vs $\sim 0.6 \mu\text{m}$). In the future it may be better to avoid polarization-based IFM detectors

since the polarization cross talk limits both the spatial resolution (see Appendix A) and the minimum noise of the detector.

For practical applications the greatest benefit will be obtained by incorporating imaging into a high-efficiency IFM system [6,8], as it is only in these systems that the chance of a photon interacting with the object becomes vanishingly small. Because such systems are in their infancy, with current efficiencies of only 60–85% [9], the issue of incorporating imaging into these systems is nontrivial and requires further research. Aside from this, further technical improvements are conceivable: for example, the possibility of obtaining an image “all at once” using a large diameter interrogating beam and some sophisticated image-processing algorithm to infer from the interference pattern the image of the object.

Classical objects that would benefit from the reduced photon flux of interaction-free imaging include: biological systems, such as cells [16], whose biological and chemical operation can change as a function of light level, and cold atom clouds, which can literally be blown apart from the photon flux of conventional imaging systems. Not only could a variety of “delicate” quantum objects (such as trapped ions, Bose-Einstein condensates, or atoms in an atom interferometer) be interaction-free imaged as well, but in high-efficiency systems the act of imaging can entangle the imaging photons and the quantum object, creating interesting quantum-mechanical states, such as entangled Schrödinger cat states [13].

The difference between conventional and interaction-free measurements of the *presence* of an object is that in the latter, in principle, the object can be detected with *no* photons interacting with the object. Similarly, the principal difference between conventional and interaction-free *imaging* of an object is the vastly reduced photon flux needed to obtain an image in the latter. Current photonic imaging systems [e.g., optical low coherence reflectometry (OLCR)] can have very high sensitivity (to opacity), say one part in 10^{12} (-120 dB). However, this is at the expense of sending 10^{12} photons *through* the imaged object and having at least one of those photons interact in a detectable fashion (e.g., in OLCR, by backscattering); of course the remaining photons can and do interact with the object in a variety of ways (general scattering, absorption, etc.). In contrast to this, we suggest that a high-efficiency interaction-free imaging system might attain high sensitivity by having only a few photons interact with the object, the rest remaining in the other arm of the interferometer; further analysis is needed to quantify this. In any event, it is clear that the techniques of interaction-free measurements and imaging, presented here and elsewhere, offer unique capabilities beyond those normally considered in conventional optics.

ACKNOWLEDGMENTS

We wish to acknowledge fruitful discussions with Anton Zeilinger, Raymond Y. Chiao, Morgan W. Mitchell, Anders Karlsson, and Gunnar Björk. We thank Sky Frostenson for performing the diffraction measurements of the objects. The participation of O.N. was funded by the Austrian Science Foundation (FWF Project No. S65-04).

APPENDIX A: IMAGE RESOLUTION

As discussed in Sec. II A, it is desirable to have a small beam waist in the region where the object is scanned, in order to obtain high spatial resolution. The diameter of a spot available from a lens is given by

$$d = \mathcal{K} \frac{f\lambda}{\phi_D}, \quad (\text{A1})$$

where f is the focal length of the lens, λ is the wavelength of the light, ϕ_D is the diameter of the clear aperture at the lens, and \mathcal{K} is a numerical factor that depends on experimental conditions and whether the diameter under consideration is the FWHM or the Gaussian diameter (where the power has fallen to $1/e^2$ of the original value). For a lens imaging an unapertured Gaussian beam, the Gaussian diameter is given by $\mathcal{K} = 4/\pi$. However, the output of our diode laser was not a clean Gaussian mode as it had internal structure (e.g., ‘picket fencing’). To reduce effects from this structure, the beam was expanded to ~ 25 mm diameter ($1/e^2$) and then a more spatially uniform subsection of the beam was selected with an iris ($\phi_D = 5$ mm) placed before the imaging lens. Under these conditions, the beam input to the iris is approximately plane wave and the factor \mathcal{K} varies as a function of the truncation of the initial beam T :

$$T = \frac{\phi_{\text{beam}}}{\phi_{\text{iris}}}, \quad (\text{A2})$$

where ϕ_{beam} is the $1/e^2$ diameter of the input beam and ϕ_{iris} is the physical diameter of the iris. To calculate FWHM diameters, the factor \mathcal{K} is given by [11]

$$\mathcal{K} = 1.029 + \frac{0.7125}{(T - 0.2161)^{2.179}} - \frac{0.6445}{(T - 0.2161)^{2.221}}. \quad (\text{A3})$$

Taking the 5 mm iris diameter as the clear aperture of the lens, the 60 mm focal length lens and initial beam diameter of $\phi_{\text{beam}} = 25$ mm yield a factor $\mathcal{K} = 1.03$. Thus the predicted minimum spot size for the system is $d = 8.3 \mu\text{m}$ (FWHM) and the predicted minimum resolution (as defined by the Rayleigh criterion [11]) is $d_R = 9.8 \mu\text{m}$.

It is possible in principle to attain a smaller spot size by increasing the diameter of the iris. However, in practice, this was limited by two experimental factors: the nonuniform beam and the angle-dependent cross talk at the polarizing beam splitters. As mentioned above, the output beam from the diode laser contained spatial structure. If the beam was unapertured the diffraction of this structure meant that the achievable fringe visibility was quite low, less than 60%; by aperturing a uniform subsection of the beam the fringe visibility was improved to 95%. This aperturing was merely for the sake of convenience and could have been avoided by a suitable mode cleaning system. However, the second effect could not have been so avoided. The cross talk on the polarizing beam splitters is a minimum when the beam passing through the device is collimated. As the beam becomes strongly diverging or converging (as was the case in our experiment), the amount of cross talk increases rapidly. This behavior occurs both for interface PBS’s (such as the cube

PBS’s we used) and for bulk PBS’s (e.g., calcite prisms). Our aperture size of 5 mm was thus chosen to give an acceptable trade-off between imaging spot size and polarization cross talk.

APPENDIX B: CALCULATING P_{IFM} FROM P_{norm}

From the normalized transmission probability P_{norm} it is straightforward to calculate the expected interaction-free measurement probability P_{IFM} as long as the reflectances R_1 and R_2 of the interferometer are known. Consider inputting linearly polarized light (at θ_1) to the polarizing Mach-Zehnder interferometer described in Sec. II A. We use a Jones matrix description, where, for example, light linearly polarized at an angle θ with respect to the vertical axis is described as

$$\begin{bmatrix} \sin \theta \\ \cos \theta \end{bmatrix}. \quad (\text{B1})$$

After passing through the interferometer the light is described by

$$\begin{bmatrix} te^{i\phi} & 0 \\ 0 & 1 \end{bmatrix} \begin{bmatrix} \sin \theta_1 \\ \cos \theta_1 \end{bmatrix}, \quad (\text{B2})$$

where t is the real part of the free-space transmittivity of the object and ϕ is the phase shift that the light acquires in its passage through the object:

$$P_{\text{norm}} = t^2. \quad (\text{B3})$$

After passing through the analyzer at angle θ_2 , the probability of an interaction-free measurement P_{IFM} , is

$$\begin{aligned} P_{\text{IFM}} &= \left| \begin{bmatrix} \sin \theta_2 & -\cos \theta_2 \\ 0 & 1 \end{bmatrix} \begin{bmatrix} te^{i\phi} & 0 \\ 0 & 1 \end{bmatrix} \begin{bmatrix} \sin \theta_1 \\ \cos \theta_1 \end{bmatrix} \right|^2 \\ &= |te^{i\phi} \sin \theta_1 \sin \theta_2 - \cos \theta_1 \cos \theta_2|^2. \end{aligned} \quad (\text{B4})$$

From this, and remembering that the effective reflectance of the first beam splitter is $R_1 = \cos^2 \theta_1$, that the transmittance of the analyzer is $T_2 = \sin^2 \theta_2$, and that $R_i + T_i = 1$, we rewrite Eq. (B4)

$$P_{\text{IFM}} = R_1 R_2 + T_1 T_2 P_{\text{norm}} - 2 \cos \phi \sqrt{R_1 R_2 T_1 T_2 P_{\text{norm}}}, \quad (\text{B5})$$

which relates P_{IFM} to P_{norm} . For the case of 50-50 beam splitters (i.e., input light polarized at $\theta_1 = 45^\circ$), this reduces to

$$P_{\text{IFM}} = \frac{1 + P_{\text{norm}} - 2 \cos \phi \sqrt{P_{\text{norm}}}}{4} = \frac{|1 - te^{i\phi}|^2}{4}. \quad (\text{B6})$$

In this case, if the object is totally opaque ($P_{\text{norm}} = 0$), then $P_{\text{IFM}} = 1/4$, as expected. (Naturally, if the object is absent then $P_{\text{norm}} = 1$, $\phi = 0$, and $P_{\text{IFM}} = 0$.) Of course, in the EV scheme considered here, the probability of the object absorbing a photon is independent of the interference conditions and in all cases is given by $P_{\text{abs}} = (1 - t^2)R_1$.

- [1] See, for example, R. P. Feynman, R. B. Leighton, and M. Sands, *The Feynman Lectures on Physics* (Addison-Wesley, Reading, MA, 1977).
- [2] M. Renninger, *Z. Phys.* **158**, 417 (1960). This is written in German. For non-German speakers, a brief and clear discussion of this paper in English is given in J. G. Cramer, *Rev. Mod. Phys.* **58**, 647 (1986).
- [3] R. H. Dicke, *Am. J. Phys.* **49**, 925 (1981).
- [4] A. C. Elitzur and L. Vaidman, *Found. Phys.* **23**, 987 (1993).
- [5] There has been some controversy and misunderstanding concerning what is meant by “interaction” in the context of “interaction-free” measurements. In particular, we stress that there must be a coupling (interaction) term in any Hamiltonian description of the IFM system. For brevity’s sake, throughout the rest of this paper we omit the quotes from “interaction-free,” although, as we shall see, they are often justified.
- [6] P. G. Kwiat, H. Weinfurter, T. Herzog, and A. Zeilinger, *Phys. Rev. Lett.* **74**, 4763 (1995).
- [7] E. H. du Marchie van Voorthuysen, *Am. J. Phys.* **64**, 1504 (1996).
- [8] H. Paul and M. Pavicic, *J. Opt. Soc. Am. B* **14**, 1275 (1997).
- [9] P. G. Kwiat, *Phys. Scr.* (to be published).
- [10] P. G. Kwiat, H. Weinfurter, and A. Zeilinger, *Sci. Am. (Int. Ed.)* **275**, 52 (1996).
- [11] *Melles Griot 1995/96 Catalog* (Melles Griot, Irvine, CA, 1996), pp. 1–24 and 2–9.
- [12] A. E. Siegman, *Lasers*, 1st ed. (University Science Books, Mill Valley, CA, 1986).
- [13] P. G. Kwiat, H. Weinfurter, and A. Zeilinger, in *Coherence and Quantum Optics VII*, edited by J. H. Eberly *et al.* (Plenum, New York, 1996), pp. 673 and 674.
- [14] A. Karlsson, G. Bjork, and E. Forsberg, *Phys. Rev. Lett.* **80**, 1198 (1998).
- [15] A. G. White, D. F. V. James, and P. G. Kwiat (unpublished).
- [16] As can be seen from the scan of the thick optical fiber, imaging thick objects that can steer the light is nontrivial. Our current system is better suited to imaging thin objects where this does not occur to any great extent, such as some varieties of cells.